

## OBSERVATIONS OF MKN 421 WITH THE MAGIC TELESCOPE

J. ALBERT<sup>A</sup>, E. ALIU<sup>B</sup>, H. ANDERHUB<sup>C</sup>, P. ANTORANZ<sup>D</sup>, A. ARMADA<sup>B</sup>, M. ASENSIO<sup>D</sup>, C. BAIXERAS<sup>E</sup>, J. A. BARRIO<sup>D</sup>, M. BARTELT<sup>F</sup>, H. BARTKO<sup>G</sup>, D. BASTIERI<sup>H</sup>, S. R. BAVIKADI<sup>I</sup>, W. BEDNAREK<sup>J</sup>, K. BERGER<sup>A</sup>, C. BIGONGIARI<sup>H</sup>, A. BILAND<sup>C</sup>, E. BISESI<sup>I</sup>, R. K. BOCK<sup>G</sup>, T. BRETZ<sup>A</sup>, I. BRITVITCH<sup>C</sup>, M. CAMARA<sup>D</sup>, A. CHILINGARIAN<sup>K</sup>, S. CIPRINI<sup>L</sup>, J. A. COARASA<sup>G</sup>, S. COMMICHAU<sup>C</sup>, J. L. CONTRERAS<sup>D</sup>, J. CORTINA<sup>B</sup>, V. CURTEF<sup>F</sup>, V. DANIELYAN<sup>K</sup>, F. DAZZI<sup>H</sup>, A. DE ANGELIS<sup>I</sup>, R. DE LOS REYES<sup>D</sup>, B. DE LOTTO<sup>I</sup>, E. DOMINGO-SANTAMARÍA<sup>B</sup>, D. DORNER<sup>A</sup>, M. DORO<sup>H</sup>, M. ERRANDO<sup>B</sup>, M. FAGIOLINI<sup>O</sup>, D. FERENC<sup>N</sup>, E. FERNÁNDEZ<sup>B</sup>, R. FIRPO<sup>B</sup>, J. FLIX<sup>B</sup>, M. V. FONSECA<sup>D</sup>, L. FONT<sup>E</sup>, M. FUCHS<sup>G</sup>, N. GALANTE<sup>O</sup>, M. GARCZARCYK<sup>G</sup>, M. GAUG<sup>H</sup>, M. GILLER<sup>J</sup>, F. GOEBEL<sup>G</sup>, D. HAKOBYAN<sup>K</sup>, M. HAYASHIDA<sup>G</sup>, T. HENGSTEBECK<sup>M</sup>, D. HÖHNE<sup>A</sup>, J. HOSE<sup>G</sup>, C. C. HSU<sup>G</sup>, P. G. ISAR<sup>G</sup>, P. JACON<sup>J</sup>, O. KALEKIN<sup>M</sup>, R. KASYRA<sup>G</sup>, D. KRANICH<sup>C,N</sup>, M. LAATIAOUI<sup>G</sup>, A. LAILLE<sup>N</sup>, T. LENISA<sup>I</sup>, P. LIEBING<sup>G</sup>, E. LINDFORS<sup>L</sup>, S. LOMBARDI<sup>H</sup>, F. LONGO<sup>P</sup>, J. LÓPEZ<sup>B</sup>, M. LÓPEZ<sup>D</sup>, E. LORENZ<sup>C,G</sup>, F. LUCARELLI<sup>D</sup>, P. MAJUMDAR<sup>G</sup>, G. MANEVA<sup>Q</sup>, K. MANNHEIM<sup>A</sup>, O. MANSUTTI<sup>I</sup>, M. MARIOTTI<sup>H</sup>, M. MARTÍNEZ<sup>B</sup>, K. MASE<sup>G</sup>, D. MAZIN<sup>G,\*</sup>, C. MERCK<sup>G</sup>, M. MEUCCI<sup>O</sup>, M. MEYER<sup>A</sup>, J. M. MIRANDA<sup>D</sup>, R. MIRZOYAN<sup>G</sup>, S. MIZOBUCHI<sup>G</sup>, A. MORALEJO<sup>B</sup>, K. NILSSON<sup>L</sup>, E. OÑA-WILHELMI<sup>B</sup>, R. ORDUÑA<sup>E</sup>, N. OTTE<sup>G</sup>, I. OYA<sup>D</sup>, D. PANEQUE<sup>G</sup>, R. PAOLETTI<sup>O</sup>, M. PASANEN<sup>L</sup>, D. PASCOLI<sup>H</sup>, F. PAUSS<sup>C</sup>, N. PAVEL<sup>M,U</sup>, R. PEGNA<sup>O</sup>, M. PERSIC<sup>R</sup>, L. PERUZZO<sup>H</sup>, A. PICCIOLI<sup>O</sup>, M. POLLER<sup>A</sup>, E. PRANDINI<sup>H</sup>, A. RAYMERS<sup>K</sup>, J. RICO<sup>B</sup>, W. RHODE<sup>F</sup>, B. RIEGEL<sup>A</sup>, M. RISSI<sup>C</sup>, A. ROBERT<sup>E</sup>, S. RÜGAMER<sup>A</sup>, A. SAGGION<sup>H</sup>, A. SÁNCHEZ<sup>E</sup>, P. SARTORI<sup>H</sup>, V. SCALZOTTO<sup>H</sup>, V. SCAPIN<sup>H</sup>, R. SCHMITT<sup>A</sup>, T. SCHWEIZER<sup>M</sup>, M. SHAYDUK<sup>M</sup>, K. SHINOZAKI<sup>G</sup>, S. N. SHORE<sup>S</sup>, N. SIDRO<sup>B</sup>, A. SILLANPÄÄ<sup>L</sup>, D. SOB CZYNSKA<sup>J</sup>, A. STAMERRA<sup>O</sup>, L. S. STARK<sup>C</sup>, L. TAKALO<sup>L</sup>, P. TEMNIKOV<sup>Q</sup>, D. TESCARO<sup>B</sup>, M. TESHIMA<sup>G</sup>, N. TONELLO<sup>G</sup>, A. TORRES<sup>E</sup>, D. F. TORRES<sup>B,T</sup>, N. TURINI<sup>O</sup>, H. VANKOV<sup>Q</sup>, V. VITALE<sup>I</sup>, R. M. WAGNER<sup>G</sup>, T. WIBIG<sup>J</sup>, W. WITTEK<sup>G</sup>, R. ZANIN<sup>H</sup>, J. ZAPATERO<sup>E</sup>

*Draft version March 20, 2006*

### ABSTRACT

The blazar Mkn 421 was observed at GeV-TeV energies during moderately high flux states between November 2004 and April 2005 with the MAGIC telescope, shortly after the end of its commissioning phase. Here we present a combined analysis of data samples recorded under different observational conditions. The integrated flux level is found to vary by more than a factor 2 on different time-scales down to 1 hour. A clear correlation is observed between  $\gamma$ -rays and X-rays fluxes, as well as a weaker correlation between  $\gamma$ -rays and optical data. The energy spectrum between 100 GeV and 3 TeV shows a clear curvature. After correcting the measured spectrum for the effect of the gamma-gamma attenuation caused by the extragalactic background light (EBL) there is an indication of an inverse Compton peak around 100 GeV, independent of the flux level.

*Subject headings:* gamma rays: observations, BL Lacertae objects: individual (Mkn 421)

### 1. INTRODUCTION

Mkn 421 (redshift  $z = 0.030$ ) is the closest known and, along with Mkn 501, the best studied TeV blazar. It was the first extragalactic  $\gamma$ -ray source detected in the TeV energy range using IACTs (Punch et al. 1992;

Petry et al. 1996). Mkn 421 is the source with the fastest observed flux variations among TeV  $\gamma$ -ray emitters. So far it showed variations larger than one order of magnitude and occasional flux doubling times as short as 15 min (Gaidos et al. 1996; Aharonian et al. 2002). Variations in the hardness of the TeV  $\gamma$ -ray spectrum during flares were reported by several groups (e.g. Krennrich et al. (2002); Aharonian et al. (2005a)). Simultaneous observations in the X-ray and GeV-TeV bands show a significant flux correlation (Krawczynski et al. 2001; Błażejowski et al. 2005).

Mkn 421 was detected and studied in all accessible wavelengths of the electromagnetic spectrum from radio to very high energy (VHE)  $\gamma$ -rays. The overall spectral energy distribution (SED) shows a typical two bump structure with the first peak in the keV energy range and the second peak at GeV-TeV energies. The SED is commonly interpreted as beamed, non-thermal emission of synchrotron and inverse-Compton radiation from ultrarelativistic electrons, accelerated by shocks moving along the jets at relativistic bulk speed. Simple one-zone synchrotron-self-Compton (SSC) models (e.g. Coppi (1992); Costamante & Ghisellini (2002)) describe the observational results satisfactorily well. However, hadronic models (Mannheim et al. 1996; Mücke et al. 2003) can explain the observed features too. A way to distinguish between the different emission models is to close some

<sup>a</sup> Universität Würzburg, D-97074 Würzburg, Germany

<sup>b</sup> Institut de Física d'Altes Energies, Edifici Cn., E-08193 Bellaterra (Barcelona), Spain

<sup>c</sup> ETH Zurich, CH-8093 Switzerland

<sup>d</sup> Universidad Complutense, E-28040 Madrid, Spain

<sup>e</sup> Universitat Autònoma de Barcelona, E-08193 Bellaterra, Spain

<sup>f</sup> Universität Dortmund, D-44227 Dortmund, Germany

<sup>g</sup> Max-Planck-Institut für Physik, D-80805 München, Germany

<sup>h</sup> Università di Padova and INFN, I-35131 Padova, Italy

<sup>i</sup> Università di Udine, and INFN Trieste, I-33100 Udine, Italy

<sup>j</sup> University of Łódź, PL-90236 Lodz, Poland

<sup>k</sup> Yerevan Physics Institute, AM-375036 Yerevan, Armenia

<sup>l</sup> Tuorla Observatory, FI-21500 Piikkiö, Finland

<sup>m</sup> Humboldt-Universität zu Berlin, D-12489 Berlin, Germany

<sup>n</sup> University of California, Davis, CA-95616-8677, USA

<sup>o</sup> Università di Siena, and INFN Pisa, I-53100 Siena, Italy

<sup>p</sup> Università di Trieste, and INFN Trieste, I-34100 Trieste, Italy

<sup>q</sup> Institute for Nuclear Research and Nuclear Energy, BG-1784 Sofia, Bulgaria

<sup>r</sup> Osservatorio Astronomico and INFN Trieste, I-34100 Trieste, Italy

<sup>s</sup> Università di Pisa, and INFN Pisa, I-56126 Pisa, Italy

<sup>t</sup> Institut de Ciències de l'Espai, E-08193 Bellaterra (Barcelona), Spain

<sup>u</sup> deceased

\* correspondence: mazin@mppmu.mpg.de

gaps in the SED, as well as to determine the position of the second peak in the SED and to obtain simultaneous, time resolved data in a broad energy range by performing multiwavelength campaigns.

The MAGIC telescope (Major Atmospheric Gamma Imaging Cherenkov telescope; see Lorenz (2004)), located on the Canary Island La Palma (2200 m asl,  $28^{\circ}45'N$ ,  $17^{\circ}54'W$ ), has completed its commissioning phase in early fall 2004. MAGIC is currently the largest imaging atmospheric Cherenkov telescope (IACT), having a 17 m diameter tessellated reflector dish consisting of 964  $0.5 \times 0.5$  m<sup>2</sup> diamond milled aluminium mirrors. Together with the current configuration of the MAGIC camera with the trigger region of 2.0 degrees diameter (Cortina et al. 2005), this results in a trigger collection area for  $\gamma$ -rays of the order of  $10^5$  m<sup>2</sup>, which further increases with the zenith angle of the observation. Presently the accessible trigger energy range spans from 50-60 GeV (at small zenith angles) up to tens of TeV. The MAGIC telescope is focused to 10 km distance – the most likely position for a 50 GeV air shower. The accuracy in reconstructing the direction of incoming  $\gamma$ -rays on an event by event basis, hereafter  $\gamma$  point spread function (PSF), is about 0.1 degrees, slightly depending on the analysis. The first physics observations in winter 2004/05 and in spring 2005 included observations of the well established TeV blazar Mkn 421. In total, 19 nights of data were taken on this source, the observation times per night ranging from 30 minutes up to 4 hours.

Here we present observational results in the energy range from 100 GeV to several TeV as measured by the MAGIC telescope. We first describe the data set and analysis techniques in section 2. In section 3, we present the results and, finally, in section 4, we interpret the results in terms of the SSC model.

## 2. OBSERVATIONS AND DATA ANALYSIS

The Mkn 421 data taken between November 2004 and April 2005 were divided into four samples. Due to changes in the hardware, data taken before and data taken after February 2005 were treated separately. Most of the data were taken at small zenith angles ( $ZA < 30^{\circ}$ ), resulting in a low trigger energy threshold. Only 1.5 h in December 2005 were taken at  $42^{\circ} < ZA < 55^{\circ}$  during simultaneous observations with the H.E.S.S. telescope system (Mazin et al. 2005). The standard operation mode for MAGIC is the ON-observation, with the center of the camera corresponding to the source position. Usually, to get a robust estimate of the background, part of the data are taken in the OFF mode, where a sky region is tracked by the telescope which resembles the region around the source with respect to the level of the night sky background fluctuations. In our observations, we considered the  $\gamma$ -ray signal from Mkn 421 to be strong enough to make OFF observations dispensable. Instead, the background level was estimated from the ON data as described below. In April 2005 part of the data were taken in the wobble mode (Daum et al. 1997). In this mode, two sky directions, opposite and  $0.4^{\circ}$  off source each, were tracked alternately for 20 minutes each. The advantage of the wobble tracking mode is the simultaneous measurement of the background, and thus *a priori* no need for additional OFF data. The definition of the 4 data samples is summarized in Table 1. For each

data sample a separate Monte-Carlo (MC) set of  $\gamma$  events was simulated (CORSIKA version 6.023, Knapp & Heck (2004); Majumdar et al. (2005)), taking into account the zenith angle of observation, the observational mode, and the hardware setup of the telescope.

The full data set corresponds to 29.0 hours. Runs with problems in the hardware or unusual trigger rates were rejected in order to ensure a stable performance and good atmospheric conditions. Removing the corrupted runs the total observation time decreased to 25.6 h.

For calibration, image cleaning, cut optimization, and energy reconstruction the standard analysis techniques of the MAGIC telescope (Bretz 2005; Wagner et al. 2005; Gaug et al. 2005) were applied as in Albert et al. (2005). For the  $\gamma$ /hadron separation a multidimensional classification technique based on the Random Forest method (Breiman 2001; Bock et al. 2004) was used. A Random Forest (RF) is a set of classification trees which are combined to form a generalized predictor. The combination of trees is done simply by taking the classifications from all trees and calculating the mean. Classical image shape parameters (Hillas 1985) like *Width*, *Length* and *Size* were used as input parameters. The cuts for the  $\gamma$ /hadron separation were trained for each data set separately using a small fraction of randomly chosen data events to represent the background (hadrons) and the MC  $\gamma$  events. The cuts were then chosen such that the overall cut efficiency for MC  $\gamma$  events is about 50%. The corresponding hadron suppression is about 90-99%, and it is improving with increasing *Size* of the events.

The angle between the major image axis and the line connecting the center of gravity of the image with the source position in the camera plane, called  $\alpha$ , is commonly used for stand alone IACTs to extract  $\gamma$  signal from the data. For a point source the  $\alpha$  distribution of the  $\gamma$ -like events is expected to be peaked towards low  $\alpha$  values, whereas the  $\alpha$  distribution for background events should be flat. In case of the ON-mode data, the background remaining after  $\gamma$ /hadron separation was estimated from the  $\alpha$  distribution, by performing a second order polynomial fit in the range between  $30^{\circ}$  and  $90^{\circ}$  where no  $\gamma$  events are expected (see Fig. 1). The signal was then determined as the number of observed events in the range  $\alpha < \alpha_0$  exceeding the fit extrapolated to small  $\alpha$ , where  $\alpha_0$  is energy dependent and has a typical value of  $15^{\circ}$ . The significance of an excess is calculated according to Eq. 17 in Li & Ma (1983). In the wobble mode, the ON (*source*) data are defined by calculating image parameters with respect to the source position, whereas OFF data are the same events but with image parameters calculated with respect to the position on the opposite side of the camera, i.e. *antisource* position. In order to avoid an unwanted contribution of  $\gamma$ -events in the OFF sample and guarantee the statistical independence between the ON and the OFF samples in the signal region the following procedure is applied: events with  $\alpha_{source} < \alpha_0$ , with  $\alpha_{source}$  calculated with respect to the source position, are excluded from the OFF sample, and events with  $\alpha_{antisource} < \alpha_0$ , with  $\alpha_{antisource}$  calculated with respect to the antisource position, are excluded from the ON sample. This cut assures that the  $\alpha$  distributions for ON and OFF events are statistically independent for  $\alpha < \alpha_0$ . The  $\alpha$  approach was used to determine the excess events for all four data sets (Table 1).

As an alternative to this classical  $\alpha$  approach, the so-called  $\theta^2$  approach can be applied, more common for the analysis of data from a system of IACTs like HEGRA or H.E.S.S. The angle  $\theta$  denotes the angular distance between the source position and the reconstructed arrival direction of the air shower. Since for a single IACT the angle  $\theta$  cannot be reconstructed directly, the so-called DISP method (Fomin et al. 1994; Lessard et al. 2001; Domingo-Santamaría et al. 2005) was used to determine the source position in the camera plane, using image shape parameters. Then, similar to the  $\alpha$  approach, the number of excess events is determined as the difference between the source and background region  $\theta^2$  distributions. An advantage of the  $\theta^2$  approach is a possibility to produce sky maps in which for every  $\gamma$ -ray candidate an origin in the sky can be assigned (see Fig. 3). The background-subtracted  $\theta^2$  distribution for samples III and IV is shown in Fig. 2. The average background was estimated from the wobble data themselves, by excluding the sector of the camera affected by the presence of the strong source. The solid line in Fig. 2 indicates the expectation from MC- $\gamma$  events for a point source.

These conservative analyses are known to produce results above 100 GeV. The energy regime below 100 GeV will require additional studies, in particular concerning the background rejection. Thus, in our sample the *Size* parameter (total amount of light of the image and in first order proportional to the energy) was required to be above 150 photoelectrons.

The energy estimation was performed using again the Random Forest technique, based on the image parameters of a MC  $\gamma$  sample. This sample is statistically independent of the one used for the training of the gamma/hadron separation cuts. Prior to the training of the energy estimation, loose cuts were applied to avoid a possible bias caused by  $\gamma$  events with outlying parameters. The energy thresholds of the individual analyses (as given in Table 1) are defined as the peak in the differential energy distribution of the MC- $\gamma$  events after all cuts. Our analyses showed that we were able to extract excess events with energies  $\sim 50$  GeV lower than the corresponding peak value. The number of excess events in bins of true energy is determined from the number of excess events in bins of the estimated energy by applying an unfolding. Unfolding is a procedure to correct the experimental energy for the effects of the finite energy resolution. In this analysis the unfolding was carried out using a method similar to those described in Anykeyev et al. (1991). Finally, the flux is determined by dividing the number of excess events by the effective observation time and the effective collection area.

### 3. RESULTS

#### *SIGNAL*

During the entire observation period Mkn 421 was found to be in a moderate to high flux state, resulting in clear signals in all four data samples. Fig. 1 shows the  $\alpha$  distribution of the  $\gamma$ -candidates of the combined samples I, II, and III with an energy threshold of  $\sim 150$  GeV. An excess of about 7000 events was found, which, for the given background, corresponds to more than 49 standard deviations. The number of excess events and the significances for the individual samples are summarized in Table 1. Fig. 3 shows a sky map produced with the DISP method using samples III and IV. The reconstructed source position from the sky map (Fig. 3, indicated by the black cross) is centered at RA=+11h04'19'', DEC=38°11'41''. The systematic error of the pointing is 2' and much larger than the statistical errors. The  $\gamma$  PSF is indicated by a white circle in the left bottom corner. The observed extension of Mkn 421 is compatible with the MC expectation of a point source which can also be seen in Fig. 2.

#### *LIGHTCURVE*

The integral fluxes above 200 GeV, averaged over each night of observation, are shown in the upper part of Fig. 4. Significant variations of up to a factor of four overall and up to a factor two in between successive days can be seen. Since sample II has an energy threshold of 260 GeV it is not shown on the lightcurve. The relatively high analysis energy threshold of 200 GeV applied for the lightcurve ensures that the results are independent of the actual trigger thresholds during each night. In the middle part of Fig. 4 the corresponding flux in the X-ray band as observed by the All-Sky-Monitor (ASM<sup>1</sup>) on-board the RXTE satellite is shown. In the lower panel of Fig. 4 the optical data taken by the KVA telescope on La Palma (<http://tur3.tur.iac.es/>) are shown. Note that the contribution of the host galaxy (appr. 8.0 mJy) has been subtracted. While the X-ray data show a moderate variability within the observation period, the optical flux stays almost constant.

For the night of highest activity in April (around midnight 53465) the lightcurve of the MAGIC data are shown in Fig. 5 and in Fig. 6 in bins of 10 minutes. The intra-night variability in the energy bin 200 to 400 GeV (Fig. 5) is not significant. A fit by a constant leads to a probability of 36% and a reduced  $\chi^2$  of 0.85. The lightcurve for the higher energy bin  $E > 400$  GeV (Fig. 6) can also be fitted by a constant with a probability of 10% and a reduced  $\chi^2$  of 1.5. Combining the findings from the intra-night lightcurves we conclude that we did not find strong evidence for flux variability within individual nights despite the high sensitivity of MAGIC for this search.

#### *ENERGY SPECTRUM*

#### *MEASURED SPECTRUM*

For the spectrum calculation, the data taken between December 2004 and April 2005 have been divided into a high and a low flux state (highest 5 and lowest 8 nights in Fig. 4). The corresponding differential energy spectra

<sup>1</sup> [http://heasarc.gsfc.nasa.gov/xte\\_weather/](http://heasarc.gsfc.nasa.gov/xte_weather/)

are shown in Fig. 7. The energy spectra extend from around 100 GeV to several TeV. The error bars shown are statistical only. Systematic errors are estimated to be 35% on the absolute flux level. The resulting spectra in high and low states differ by a factor 1.45 in absolute flux level whereas their shapes are compatible within the errors: The reduced  $\chi^2$  (after renormalization) between the two spectra is 1.38. Since the slope differences between the high and low-state spectrum are only marginal we combine the data sets for the further discussion.

#### ABSORPTION BY THE EBL

The VHE photons from Mkn 421 cross  $\sim 400$  million light years on their way to Earth. On their way they interact with the low energy photons of the extragalactic background light (EBL, see Nikishov (1962); Gould & Schröder (1966); Stecker et al. (1992); Hauser & Dwek (2001)) consisting of redshifted star light of all epochs and reemission of a part of this light by dust in galaxies. The most common reaction channel between VHE  $\gamma$ -rays and the low energy photons of the EBL is pair production when the center of mass energy is large enough to produce electron positron pairs:  $\gamma_{\text{VHE}} + \gamma_{\text{EBL}} \rightarrow e^+ e^-$ . The intrinsic (de-absorbed) photon spectrum,  $dN/dE_i$ , of a blazar located at redshift  $z$  is given by:

$$dN/dE_i = dN/dE_{\text{obs}} \times \exp[\tau_{\gamma\gamma}(E, z)],$$

where  $dN/dE_{\text{obs}}$  is the observed spectrum and  $\tau_{\gamma\gamma}(E, z)$  is the optical depth. The distance to Mkn 421 implies that the optical depth (e.g. Eq. 2 in Dwek & Krennrich (2005)) strongly depends on the shape and absolute level of the EBL between 1 and 30  $\mu\text{m}$ . A rather complicated distortion of the intrinsic spectrum takes place above  $\sim 100$  GeV. Although the calculation of the optical depth is straight forward the spectral energy distribution of the EBL is uncertain. Direct measurements of the EBL are difficult because of the strong foreground emission consisting of reflected sunlight and thermal emission from zodiacal dust particles. Hence many measurements lead to upper limits (Hauser et al. 1998; Dwek & Arendt 1998). Several measurements claimed a direct detection of the EBL but some of them are controversial (Matsumoto et al. 2005; Finkbeiner et al. 2000). An alternative method to determine the EBL are fluctuation analyses of the measured radiation. Since a part of the EBL originates from discrete sources, then fluctuations in the number of sources in an observer's field of view will produce fluctuations in the measured background (Kashlinsky et al. 1996; Kashlinsky & Odenwald 2000). A third method are the galaxy counts in the deep field surveys which provide robust lower limit to the SED of the EBL (Elbaz et al. 2002; Metcalfe et al. 2003; Fazio et al. 2004; Madau & Pozzetti 2000). The results of these methods are summarized in Fig. 8. It is notable that present detections of the EBL and the independently determined upper and lower limits are not in conflict with each other. However, the uncertainty of the present measurements allow a range of the EBL levels differing by a factor 2 to 4 depending on the wavelength. Several attempts were also made to model the evolution of the EBL and its present state (see Hauser & Dwek (2001) for summary). The models which are made to predict the EBL today tend to lie close to the galaxy

counts in the optical – near-infrared and somehow underestimate the EBL in mid- and far-infrared which might be related to higher content of dust in earlier galaxies than in the nearby galaxies. Here we adopt the recent model of Primack et al. (2005) but scale it up by a factor 1.5 (which is within the model uncertainties) to match lower limits set by *Spitzer* mission and ISOCAM in the range 4 to 15  $\mu\text{m}$  (Fazio et al. 2004; Elbaz et al. 2002; Metcalfe et al. 2003). The resulting EBL spectrum is shown in Fig. 8 by the black curve. This EBL spectrum agrees with alternative models (e.g. (Kneiske et al. 2004; Pei et al. 1999; Blain et al. 1999)) which are designed to predict the EBL today. It is also very close to the upper limits inferred from arguments on AGN spectra (Aharonian et al. 2005b). Using this EBL spectrum and state-of-the-art cosmology (flat universe, Hubble constant  $H_0=72$  km/s/Mpc, matter density  $\Omega_m=0.3$ , dark energy density  $\Omega_\Lambda=0.7$ ) we calculated the optical depth  $\tau_{\gamma\gamma}$  for Mkn 421. Thereby we use numerical integration of the Eq. 2 from Dwek & Krennrich (2005). The attenuation coefficient  $\exp(-\tau_{\gamma\gamma})$  is shown as the function of energy of VHE  $\gamma$ -rays in Fig. 9.

#### DE-ABSORBED SPECTRUM OF MKN 421

The measured spectrum and the reconstructed de-absorbed (i.e. corrected for the effect of intergalactic absorption) spectrum are shown in Fig. 10. Here, in order to show energy density distribution, the differential photon spectra are multiplied by  $E^2$ . The de-absorbed spectrum is clearly curved, its probability of being a simple power law is  $1.6 \times 10^{-8}$ . The de-absorbed spectrum is fitted by an exponentially cutoff power law ( $E^2 dN/dE = N_0 E^{-\alpha} \exp(-E/E_{\text{cutoff}})$ , solid line) or, alternatively, by a curved power law ( $E^2 dN/dE = N_0 E^{-\alpha_1 + \alpha_2 * \log_{10}(E/\text{TeV})}$ ), dashed-dotted line). The fit parameters are listed in the inlays of the Fig. 10. The dashed line indicates the expected absorbed spectrum using the fit values from the power law with a cut-off fit to the intrinsic SED. The power law with a cut-off as well as the curved power law fits indicate for both high and low states of Mkn 421 a flattening of the spectrum towards 100 GeV.

#### 4. DISCUSSION

The correlation between the  $\gamma$ -ray flux measured by MAGIC and the X-ray flux measured by RXTE/ASM is shown in Fig. 12. For the MAGIC flux we take the night average above 200 GeV (see also Fig. 4). For the X-ray data, we calculate the average of those RXTE/ASM pointings (dwells) which have been taken simultaneous with MAGIC data, allowing plus/minus 1 hour with respect to the MAGIC data to increase X-ray statistics. Fig. 12 shows a clear correlation between X-ray and  $\gamma$ -ray data. The linear fit (solid line) which is forced to go through (0,0) has a slope of  $1.4 \pm 0.1$  [ $\frac{10^{-10}}{\text{cm}^2} / \frac{\text{counts}}{\text{SSC}}$ ], and has a probability of being not casual of about 54%. The parabolic fit (dashed line) which is also forced to go through (0,0) has the same probability of 54% of not being casual. The correlation coefficient  $r = 0.64^{+0.15}_{-0.22}$  (errors correspond to 1 sigma level) is within 2.4 standard deviations (taking the non-linearity of errors into account) different from zero.

In Fig. 13 the MAGIC  $\gamma$ -ray flux above 200 GeV is plotted versus simultaneous KVA optical data. The latter data have been averaged over the MAGIC integration time. One can see a possible  $\gamma$ -ray/optical anticorrelation during the 8 nights of simultaneous observations. However, the correlation coefficient  $r = -0.59_{-0.22}^{+0.36}$  is within 1.5 standard deviations compatible with zero.

Given the temporal correlation between X-ray and  $\gamma$ -ray fluxes, it is reasonable to infer that the VHE  $\gamma$ -ray radiation is dominated by emission resulting from inverse-Compton (IC) upscattering of the synchrotron X-ray photons by their parent population of relativistic electrons. Such correlation can be modelled with a homogeneous synchrotron-self-Compton (SSC) model. Based on this model it is possible to constrain the parameter space of the emission region and estimate its basic parameters, the Doppler factor,  $D$ , and the rest-frame magnetic field,  $B$  of the emitting plasma in the relativistic jet. To this aim we follow the procedure first devised by Bednarek & Protheroe (1997) for Mkn 421 flare of May 16 1994 and subsequently improved by, e.g., Tavecchio et al. (1998); Bednarek & Protheroe (1999); Kataoka et al. (1999); Katarzynski et al. (2003). Application of this method requires precise simultaneous multiwavelength information. Since a synchrotron (X-ray) spectrum simultaneous with the MAGIC observations is not available, we have to resort to previous X-ray observations arguing that similar TeV  $\gamma$ -ray states (IC emission) should correspond to similar X-ray states (synchrotron emission). In fact, similar  $\gamma$ -ray spectra of Mkn 421 have been observed a few times already – including the HEGRA observations in April 1998 (Aharonian et al. 1999) for which simultaneous *BeppoSAX* observations are available (Fossati et al. 2000; Massaro et al. 2004). Here we use the X-ray spectra and parameterization, reported by Massaro et al. (2004) during for April 21, 1998. It is also noticeable that the X-ray flux level between the simultaneous RXTE/ASM data and the *BeppoSAX* data used here is very similar (see Fig. 14). The moderate flux state MAGIC  $\gamma$ -ray spectrum, reported here for energies  $\sim 100$  GeV, warrants a better investigation of the crucial energy range where IC peak is expected to occur than in previous datasets. Following Bednarek & Protheroe (1997, 1999) we then constrain the allowed parameters of the emission region ( $D$  and  $B$ ) from the ratio of the  $\gamma$ -ray power to the X-ray power, measured at their respective peak emission (see thick curves in the upper panels of Fig. 11). The radiation field density and the electron spectrum, cospatial in the blob, were derived as a function of  $D$  and  $B$  for a blob radius assumed equal to the light travel corresponding to the shortest reported variability time-scale (for observational arguments see Takahashi et al. (2000)). We further constrain the allowed parameter space by arguing that the synchrotron and IC cooling time-scales should be shorter than the observed variability time-scale. These conditions are fulfilled above the dot-dashed lines (for synchrotron cooling) and on the left of the grey dashed line (for the IC cooling) for the 1 hr (upper left panel of Fig. 11) and 1 day (upper right panel of Fig. 11) variability time-scales. The condition that the blob has to be transparent to the VHE  $\gamma$ -rays leads to a further lower bound on  $D$  by requiring that the optical depth by pair production has to be lower

than unity. The corresponding limits for photon energies of 100 GeV and 3 TeV (which define the energy range of MAGIC measurement) are shown in the upper panels of Fig. 11 as, respectively, thin dotted lines and thick dotted lines. One last condition arises from comparing the maximum energy of electrons, determined by the maximum energy of synchrotron photons  $\sim 40$  keV, with the maximum energy of the detected photons  $\sim 3$  TeV (see dashed line in the upper panels of Fig. 11). The allowed parameters of the emission region correspond to the part of the thick full curve laying inside the region limited by all these lines (see Fig. 11). In order to determine the values of  $D$  and  $B$  more precisely, we now calculate the  $\gamma$ -ray spectra for the points A, B, and C for 1 hr variability, and the points D, E, and F for 1 day variability, and compare the predicted spectrum with the actual de-absorbed spectrum. From the lower panels of Fig. 11 it is clear that the best description is provided by the blob with Doppler factor  $D \sim 22$  and magnetic field  $B \sim 0.7$  G (the point B) for 1 hr variability, and  $D \sim 9$  and  $B \sim 0.3$  G (the point D) for 1 day variability. In order to assess how this result is sensitive on the correct energy localization of the peak in the  $\gamma$ -ray spectrum (which is in fact only limited by the lower energy end of the MAGIC spectrum), we show the allowed parameter space for the  $\gamma$ -ray peak at 10 GeV (see thin full curves in Fig. 11). The constraints for the peak at 10 GeV and 100 GeV are almost the same for the parts of the curves inside the allowed region. It is interesting that the emission parameters, as estimated here for the moderate flux state of Mkn 421 (for the 1 day variability time-scale), are not very different from those estimated by Bednarek & Protheroe (1997) for the flaring state. This suggest that the flaring state may not be related to the significant change of the blob's Doppler factor and magnetic field strength. In Fig. 14 we show the broadband SED of Mkn 421. Large symbols represent averaged data described in this paper: optical data from KVA (star), X-rays from RXTE/ASM (full square),  $\gamma$ -rays from MAGIC (full points). The grey curve in the X-rays correspond to a log-parabolic fit performed by Massaro et al. (2004) on *BeppoSAX* data of Mkn 421 taken on April 21, 1998. The two black curves through the  $\gamma$ -ray spectrum are almost indistinguishable and correspond to the best SSC model parameters for 1-hr and 1-day variability time-scales (points B and D respectively).

In addition, we test the SSC code provided by Krawczynski et al. (2004) with our dataset. The fitted overall SED is shown by the grey dashed line in Fig. 14, and the model parameters are listed in Table 2. These parameters are similar to those of Krawczynski et al. (2001), although the emitting region is somewhat smaller ( $2.3 \times 10^{13}$  instead of  $2.7 \times 10^{13}$  m) and particle density is higher ( $0.03$  erg/cm<sup>3</sup> instead of  $0.01$  erg/cm<sup>3</sup>). We note that the fitted values of magnetic field and Doppler factor are within the allowed range as defined above.

## 5. CONCLUDING REMARKS

Mkn 421 was observed with the MAGIC telescope during several months in 2004 and 2005. The data were used to produce the first energy spectrum of this source extending down to 100 GeV using an IACT. The flux state was found to be moderate and ranging in intensity between 0.5 and 2 crab units. Upon splitting the data

into higher and lower states we found that the two subsets differed by a factor 1.45 in absolute flux level while they hardly differed in shape. The integrated flux level was observed to vary by up to a factor 2 between successive days, while the intra-night lightcurve, binned in 10-minute time intervals, does not show significant variations on the time-scales below 1 day. However, at higher energies the emission appears to be slightly more variable than at lower energies. We note that MAGIC is sensitive enough to detect variabilities on the 10-minute time-scale at such moderate flux level. A clear correlation between X-rays and  $\gamma$ -rays was found, while no significant correlation was seen between optical and  $\gamma$ -rays. This supports a leptonic origin of the  $\gamma$ -rays from Mkn 421. The energy spectrum resulting from the combined MAGIC data, corrected for the extragalactic absorption, suggests the presence of an IC peak at about 100 GeV. The overall SED observed in the moderate flux state can be well described by a homogeneous SSC model provided that the emission

region moves with a Doppler factor  $\sim 9$  and its magnetic field strength is  $\sim 0.3$  G for a 1-day variability time-scale. Surprisingly, these parameters do not differ substantially from those estimated for the emission region of Mkn 421 during a strong flare (Bednarek & Protheroe 1997). The fit with an alternative SSC code of Krawczynski et al. (2001) lead to similar Doppler factor and magnetic field values.

#### ACKNOWLEDGEMENTS

We would like to thank the IAC for the excellent working conditions at the Observatorio de los Muchachos in La Palma. The support of the German BMBF and MPG, the Italian INFN and the Spanish CICYT is gratefully acknowledged. This work was also supported by ETH Research Grant TH 34/04 3 and the Polish MNiI Grant 1P03D01028.

#### REFERENCES

- Aharonian, F. et al. (HEGRA Collab.), 1999, *A&A*, 350, 757.  
 Aharonian, F. et al. (HEGRA Collab.), 2002, *A&A*, 393, 89.  
 Aharonian, F. et al. (H.E.S.S. Collab.), 2005a, *A&A*, 437, 95.  
 Aharonian, F. et al. (H.E.S.S. Collab.), 2005b, submitted to *Nature*, astro-ph/0508073.  
 Albert, J. et al. (MAGIC Collab.), 2006, *ApJ*, 637, L41.  
 Anykeyev, V.B. et al., 1991, *Nucl. Instrum. Methods A*, 303, 350.  
 Bednarek, W., Protheroe, R.J., 1997, *MNRAS*, 292, 646.  
 Bednarek, W., Protheroe, R.J., 1999, *MNRAS*, 310, 577.  
 Bernstein, R. et al., 2002, *ApJ*, 571, 56,85,107.  
 Bernstein, R. et al., 2005, *ApJ*, 632, 713.  
 Blain, A.W. et al., 1999, *MNRAS*, 309, 715.  
 Błażejowski, H. et al., 2005, *ApJ*, 630, 130.  
 Bock, R.K. et al., 2004, *Nucl. Instrum. Methods A*, 516, 511.  
 Boella, G. et al., 1997, *A&A*, 122, 299.  
 Breiman, L., 2001, *Machine Learning*, 45, 5  
 Bretz, T. (for the MAGIC Collab.), *AIP Conf. Proc.*, 2005, 745, 730.  
 Cambrésy, L. et al., 2001, *ApJ*, 555, 563.  
 Cortina, J. et al. (MAGIC Collab.), *Proc. of the 29th ICRC, Pune, India*, in press, astro-ph/0508274.  
 Costamante, L. & Ghisellini, G., 2002, *A&A*, 384, 56.  
 Coppi, P.S., 1992, *MNRAS*, 258, 657.  
 Daum, A. et al. (HEGRA Collab.), 1997, *Astropart. Phys.*, 8, 1.  
 Domingo-Santamaría, E. et al. (MAGIC Collab.), *Proc. of the 29th ICRC, Pune, India*, in press, astro-ph/0508274.  
 Dwek, E. & Arendt, R.G., 1998, *ApJ*, 508, L9.  
 Dwek, E. & Krennrich, F., 2005, *ApJ*, 618, 657.  
 Elbaz, D. et al., 2002, *A&A*, 384, 848.  
 Fazio, G.G. et al., 2004, *ApJSS*, 154, 39.  
 Finkbeiner et al., 2000, *ApJ*, 544, 81.  
 Fomin, V. P. et al., 1994, *Astropart. Phys.*, 2, 137.  
 Fossati, G. et al., 2000, *ApJ*, 541, 166.  
 Gaidos, J. A. et al., 1996, *Nature*, 383, 319.  
 Gaug, M. et al. (MAGIC Collab.), *Proc. of the 29th ICRC, Pune, India*, in press, astro-ph/0508274.  
 Gorjian, V. et al., 2000, *ApJ*, 536, 550.  
 Gould, R.J. & Schröder, 1966, *Phys. Rev. Lett.*, 16, 252.  
 Hauser M.G. et al., 1998, *ApJ*, 508, 25.  
 Hauser, M.G. & Dwek, E. 2001, *ARA&A*, 39, 249.  
 Hillas, A. M., 1985, *Proc. of the 19th ICRC, La Jolla*.  
 Kashlinsky, A. et al., 1996, *ApJ*, 470, 681.  
 Kashlinsky, A. & Odenwald, S., 2000, *ApJ*, 528, 74.  
 Knapp, J. & Heck, D., 2004, *EAS Simulation with CORSIKA: A Users Manual*.  
 Kneiske, T. M. et al., 2004, *A&A*, 413, 807.  
 Kataoka, J. et al., 1999, *ApJ*, 514, 138.  
 Katarzyński, K., Sol, H., Kus, A. 2003, *A&A*, 410, 101.  
 Krennrich, F. et al., 2002, *ApJ*, 575, 9.  
 Krawczynski, H. et al., 2001, *ApJ*, 559, 187.  
 Krawczynski, H. et al., 2004, *ApJ*, 601, 151.  
 Lagache, G. et al., 2000, *A&A*, 354, 247.  
 Lessard, R. W. et al., 2001, *Astropart. Phys.*, 15, 1.  
 Lorenz, E., *New Astron. Rev.*, 2004, 48, 339.  
 Li and Ma, 1983, *ApJ*, 272, 317.  
 Mannheim, K. et al., 1996, *A&A*, 315, 77.  
 Madau, P. & Pozzetti, L., 2000, *MNRAS*, 312, L9.  
 Majumdar, P. et al., *Proc. of the 29th ICRC, Pune, India*, in press, astro-ph/0508274.  
 Martin, C., 1991, *ApJ*, 379, 549.  
 Massaro, E., 2004, *A&A*, 413, 489.  
 Matsumoto, T. et al., 2005, *ApJ*, 626, 31.  
 Mazin, D. et al., *Proc. of the 29th ICRC, Pune, India*, in press, astro-ph/0508273.  
 Metcalfe, L. et al., 2003, *A&A*, 407, 791.  
 Mücke, A. et al., 2003, *Astropart. Phys.*, 18, 593.  
 Nikishov, A.I., 1962, *Sov. Phys. JETP*, 14, 393.  
 Papovich, C. et al., 2004, *ApJSS*, 154, 70.  
 Pei, Y.C. et al., 1999, *ApJ*, 522, 604.  
 Petry, D. et al., 1996, *A&A*, 311, L13.  
 Primack, J. et al., *AIP Conf. Proc.*, 2005, 745, 23.  
 Punch, M. et al., 1992, *Nature*, 358, 477.  
 Stecker, F.W., De Jager, O.C., Salamon, M.H., 1992, *ApJ*, 390, L49.  
 Takahashi, T. et al, 2000, *ApJ*, 542, L105.  
 Tavecchio, F., Maraschi, L., Ghisellini, G., 1998, *ApJ*, 509, 608.  
 Wagner, R.M. et al. (MAGIC Collab.), *Proc. of the 29th ICRC, Pune, India*, in press, astro-ph/0508274.  
 Wright, E.L. et al., 2001, *ApJ*, 553, 538.  
 Wright, E.L. & Reese, E.D., 2000, *ApJ*, 545, 43.

TABLE 1  
RESULTS OF THE MKN 421 DATA USING THE  $\alpha$  APPROACH (SEE TEXT FOR DETAILS). SAMPLES I+II WERE RECORDED IN NOVEMBER 2004 - JANUARY 2005, WHILE SAMPLES III+IV WERE TAKEN IN APRIL 2005.

sample	on time	zenith [°]	mode	$E_{thr}$ [GeV]	$N_{on}$	$N_{off}$	$N_{excess}$	sigma
I	4.63 h	9.3 - 31.2	ON	150	3761	$1878 \pm 32$	$1883 \pm 69$	29.3
II	1.53 h	42.4 - 55.0	ON	260	1086	$674 \pm 25$	$413 \pm 41$	10.1
III	9.30 h	9.2 - 27.5	ON	150	8083	$4360 \pm 49$	$3723 \pm 102$	38.9
IV	10.12 h	9.4 - 32.4	wobble	150	7740	$4532 \pm 67$	$3208 \pm 111$	29.1

TABLE 2  
SSC MODEL PARAMETERS FOR MKN 421. THE CORRESPONDING PHOTON SPECTRUM IS SHOWN IN FIG. 14.

Doppler factor	50
magnetic field	0.22 Gaus
radius of emitting region	$2.3 \times 10^{13}$ m
electron energy density	$0.03 \text{ erg/cm}^3$
electron spectrum	
$6 < \log(E[\text{eV}]) < 10.1$	spec. index 2
$10.1 < \log(E[\text{eV}]) < 11$	spec. index 3

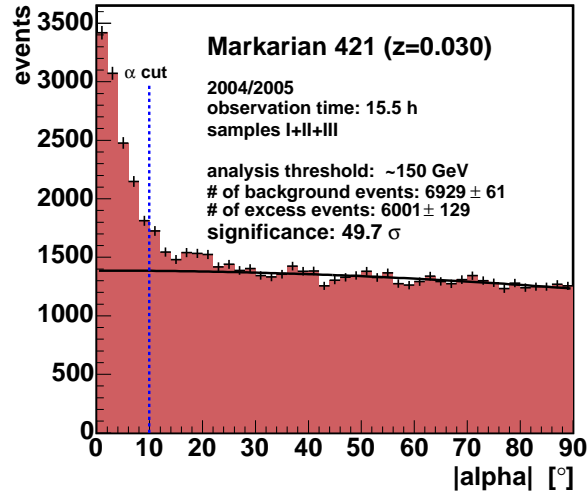


FIG. 1.—  $\alpha$  distribution for the combined data samples I+II+III with  $E_{thresh} = 150$  GeV. A vertical line indicates the  $\alpha$  cut used to extract excess events. Black parabola is a fit to the  $\alpha$  distribution between 30 and 90 degrees and it is used to estimate the background level between 0 and 10 degrees.

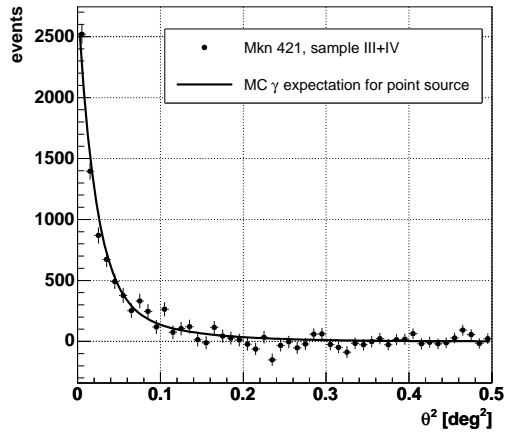


FIG. 2.—  $\theta^2$  distribution for the combined data samples III+IV with  $E_{threshold} = 150$  GeV. Background is subtracted. Black line is the MC- $\gamma$  expectation for a point source.

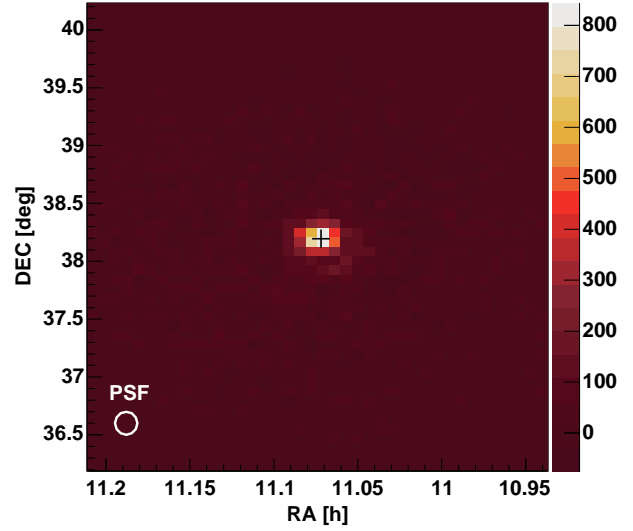


FIG. 3.— Sky map of excess events in the region of Mkn 421 for samples III+IV using the DISP method (Domingo-Santamaría et al. 2005). The black cross indicates the reconstructed source position.

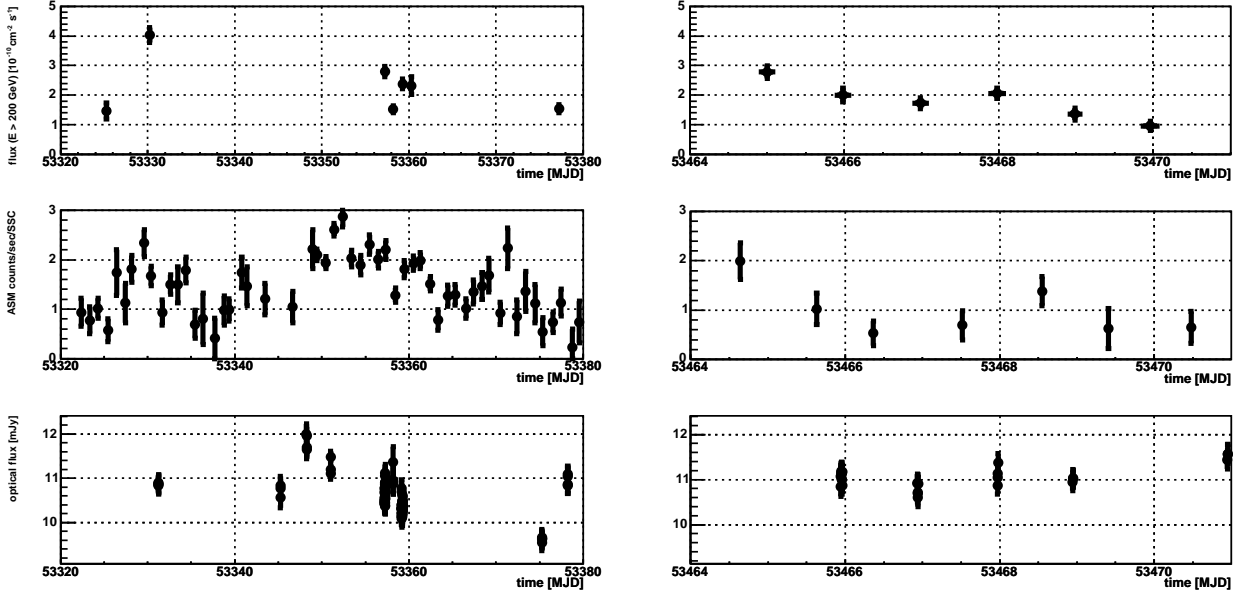


FIG. 4.— Lightcurve for Mkn 421 from November 2004 to April 2005. Left panels: data from November 2004 to January 2005. Right panels: data for April 2005. Upper panel: MAGIC data, night average of Mkn 421 above 200 GeV using samples I+III+IV. Middle panel: corresponding day-by-day X-ray counts as observed by the RXTE/ASM. Lower panel: Lightcurve of the optical flux of Mkn 421 as measured by the KVA telescope.

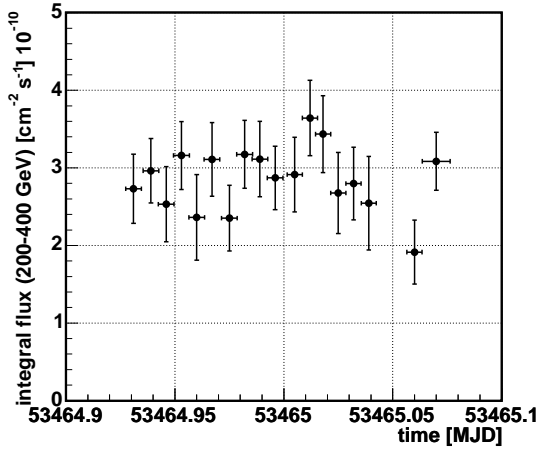


FIG. 5.— Lightcurve for the night MJD 53465 in bins of 10 minutes, integral flux 200 to 400 GeV.

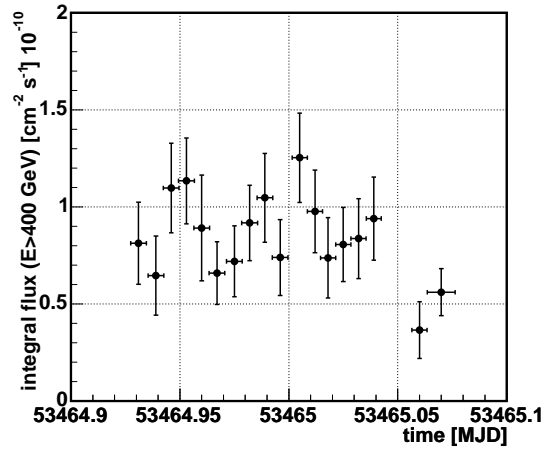


FIG. 6.— Light-curve for the night MJD 53465 in bins of 10 minutes above 400 GeV.

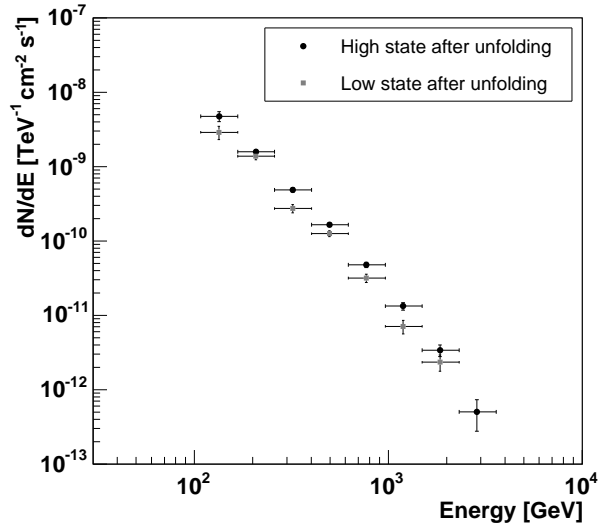


FIG. 7.— Differential energy distribution for Mkn 421 for high (black points) and low (grey squares) flux samples as described in the text.

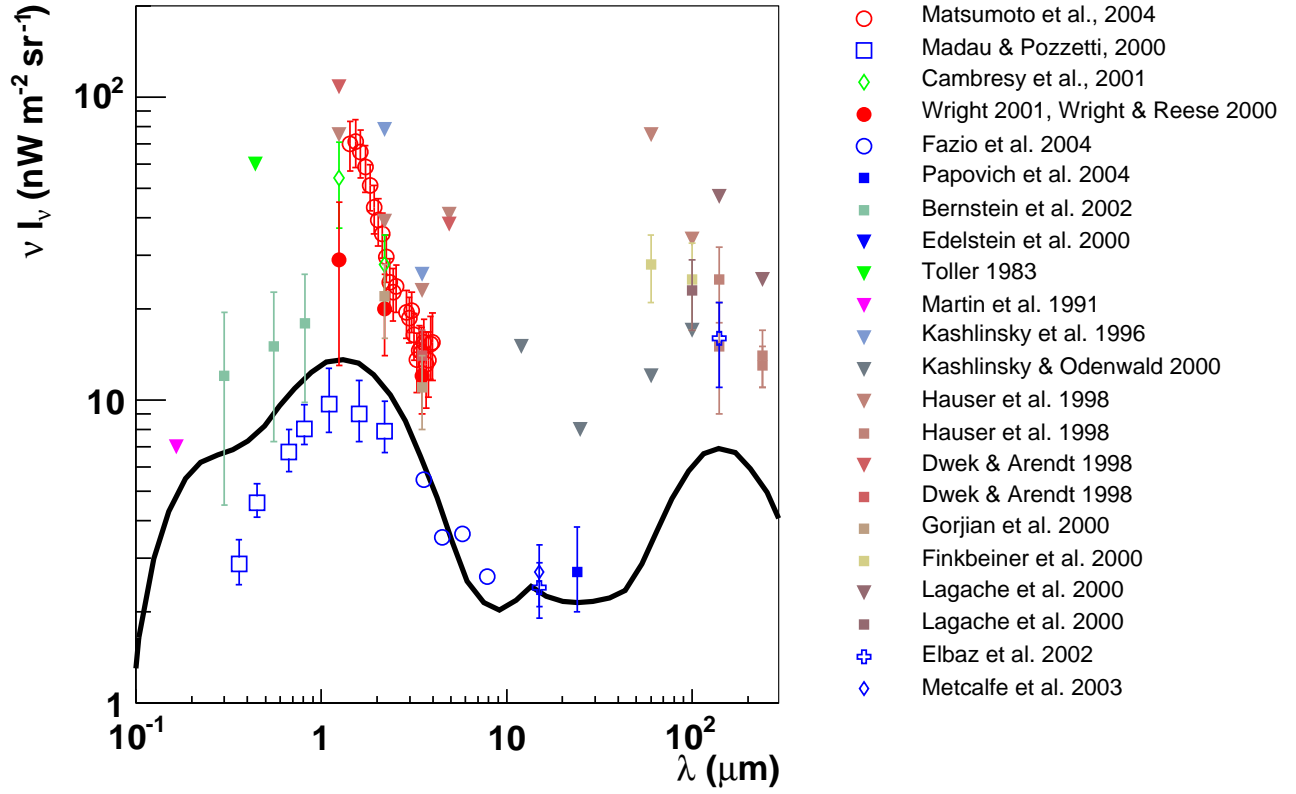


FIG. 8.— Energy density of the extragalactic background light (EBL). Direct measurements, galaxy counts, low and upper limits are shown by different symbols as described in the legend. The black curve is the EBL spectrum as in Primack et al. (2005) for  $z=0$  but scaled up by a factor 1.5 to match low limits derived from the galaxy counts (Elbaz et al. 2002; Metcalfe et al. 2003; Fazio et al. 2004).

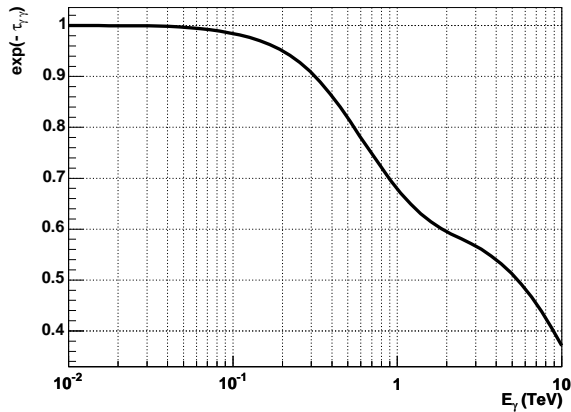


FIG. 9.— Attenuation coefficient  $\exp(-\tau_{\gamma\gamma})$  for Mkn 421 ( $z=0.030$ ) using the EBL spectrum as shown in Fig. 8.

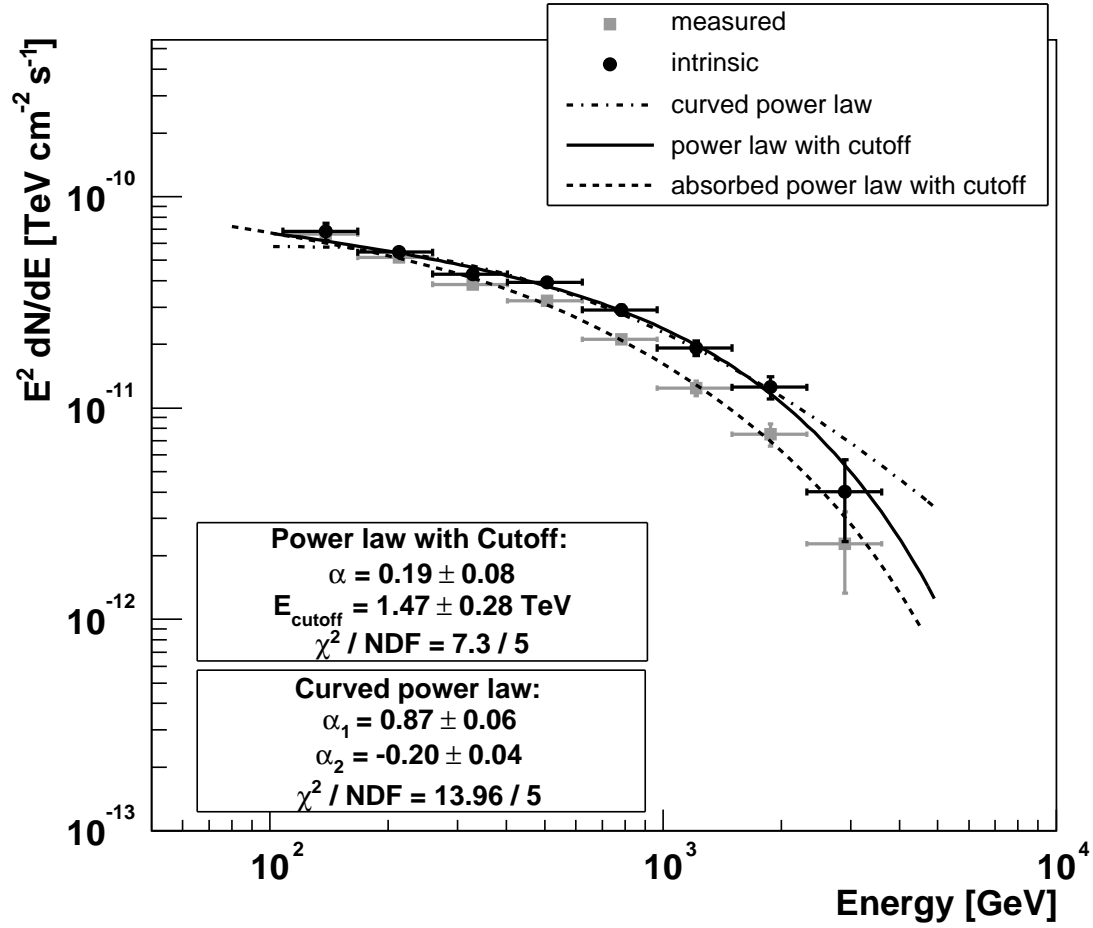


FIG. 10.— The measured (grey points) and de-absorbed (black points) spectrum of Mkn 421, multiplied by  $E^2$ . Solid line: fit (1) to the intrinsic spectrum using a power law with a cut-off. Dashed-dotted line: fit (2) to the intrinsic spectrum using a curved power law. A dashed line indicates the expected absorbed spectrum using the result of fit (1). Fit parameters of the intrinsic spectrum are shown in the inlays.

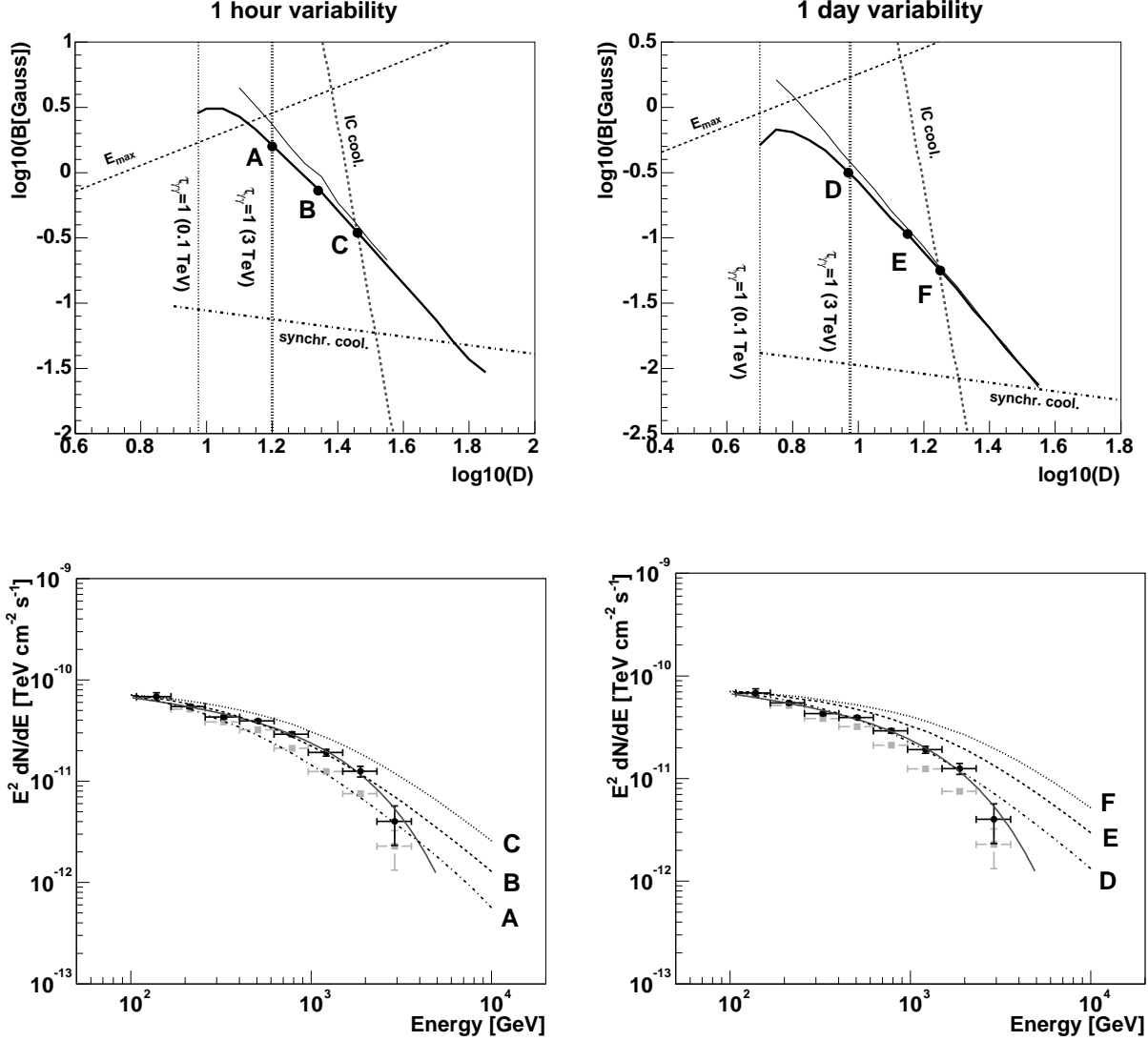


FIG. 11.— Constraints on the parameter space (Doppler factor versus magnetic field strength) for the emission region in the jet of Mkn 421 based on the homogeneous SSC model. From the ratio of the  $\gamma$ -ray to X-ray power during the MAGIC observations of Mkn 421 (measured at the peaks in the synchrotron and IC spectra) the allowed values are limited to the thick curves. The conditions for efficient electron cooling on the synchrotron and IC processes during the time of 1 hr (left figure) and 1 day (right figure) are marked by the black dot-dashed and grey dashed lines, respectively. The condition that the optical depth for  $\gamma$ -rays with energies 100 GeV and 3 TeV in the synchrotron radiation equals unity gives the lower limit on the Doppler factor of the emission region marked by the thin and thick dotted lines, respectively. The condition that maximum energy of electrons emitting synchrotron photons must be higher than the maximum energy of  $\gamma$ -rays is marked by the dashed line. The allowed region is limited by these lines. The  $\gamma$ -ray spectra are calculated for the values of the Doppler factor and magnetic field strength marked by A, B, and C (for 1 hr variability), and D, E, and F (for 1 day variability). They are compared with the MAGIC spectrum in the bottom figures.

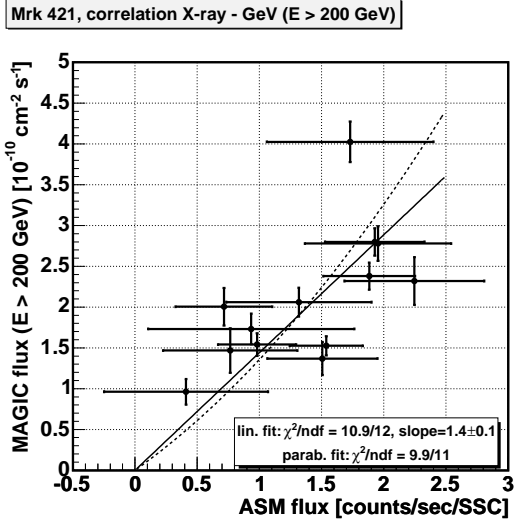


FIG. 12.— Correlation plot between MAGIC integral flux above 200 GeV and RXTE/ASM counts for 11 nights.

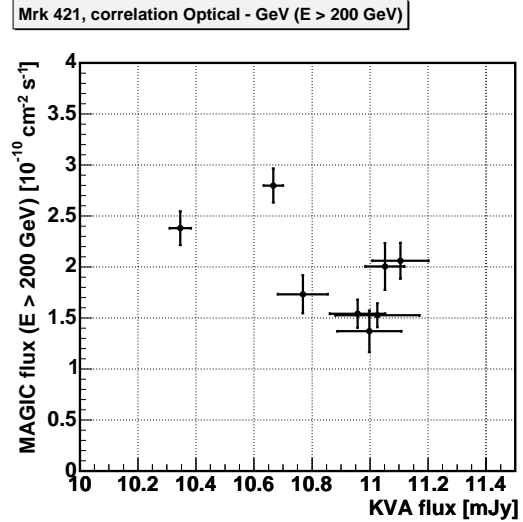


FIG. 13.— Correlation plot between MAGIC integral flux above 200 GeV and optical data from KVA telescope for 8 nights.

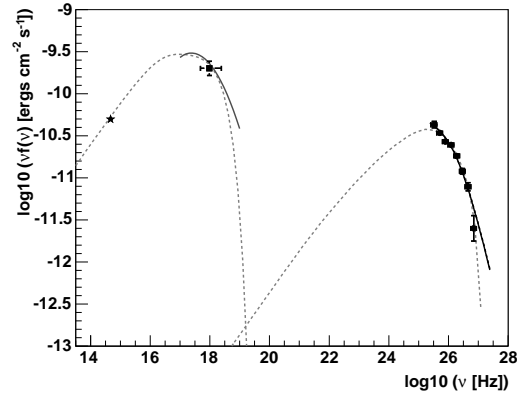


FIG. 14.— The overall optical through VHE  $\gamma$ -ray SED of Mkn 421. Large symbols represent averaged data described in this paper: optical data from KVA (star), X-rays from RXTE/ASM (full square), de-absorbed  $\gamma$ -rays from MAGIC (full points). The grey curve in the X-rays correspond to the log-parabolic fit taken from Massaro et al. (2004) using *BeppoSAX* (Boella 1997) data of Mkn 421 taken on April 21, 1998. The two black curves through the  $\gamma$ -ray spectrum (almost indistinguishable) correspond to the SSC model parameters B and D (see text and Fig. 11 for details). The dashed line is SSC model as in Krawczynski et al. (2004), see text for details.